THE JOURNAL OF PHYSICAL CHEMISTRY C

Article

Cite This: J. Phys. Chem. C 2018, 122, 24559−24569

pubs.acs.org/JPCC

Operando Studies Reveal Structural Evolution with Electrochemical Cycling in Li−CoS_2

Megan M. Butala,*[,†,§] Vicky V. T. Doan-Nguyen,[‡] Anna J. Lehner,[§,∥] Claudia Göbel,[§] Margaret A. Lumley,[§] Shiri Arnon,[§] Kamila M. Wiaderek,[⊥] Olaf J. Borkiewicz,[⊥] Karena W. Chapman,[⊥] Peter J. Chupas,[⊥] Mahalingam Balasubramanian,[⊥] and Ram Seshadri*[,†,§]

[†]Mitsubishi Chemical Center for Advanced Materials, [§]Materials Research Laboratory, Materials Department, and [‡]California NanoSystems Institute, University of California, Santa Barbara, California 93106, United States

[∥]Fraunhofer IWM, 79108 Freiburg, Germany

[⊥]X-ray Science Division, Advanced Photon Source, Argonne National Laboratory, Argonne, Illinois 60439, United States

ABSTRACT: The drive toward high energy density alternatives to Li-ion batteries has led to great interest in energy storage materials not inherently constrained by the capacity limits of the currently employed intercalation electrode materials. Among the alternatives under consideration are electrode materials with theoretical capacities many times greater than intercalation electrodes that store charge through so-called conversion reactions. However, the significant structural changes that enable the high theoretical capacity of conversion systems contribute to issues of poor efficiency and short cycle life. To better understand cycling issues in conversion systems, we study the local structure evolution of CoS_2 during Li storage. Being metallic and potentially capable of redox on both anion and cation sites, CoS_2 would be expected to display promise as a cathode material. Through combined ex situ X-ray absorption near-edge spectroscopy and pair distribution function analysis from operando X-ray total scattering, we describe the reactions that take place over the first 1.5 cycles. In doing so, we identify the irreversible formation of a Co_9S_8-like local structure with significantly limited electrochemical activity as the primary source of capacity fade. The methods employed here and the insights that emerge could inform the rational design of conversion systems for electrochemical energy storage.

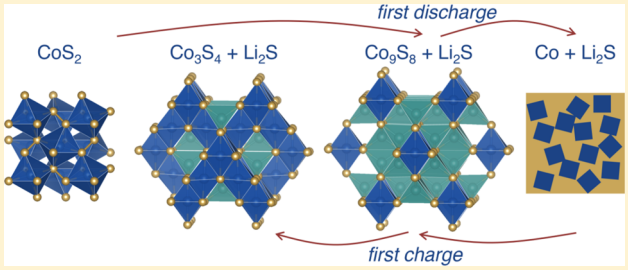

1. INTRODUCTION

Lithium-ion batteries (LIBs) are ubiquitous in portable electronics and increasingly important for large-scale applications, such as grid-scale storage. While performance improvements are still being achieved for well-studied intercalation-type electrode materials that enable commercial LIBs, these improvements are incremental and approaching their physical limits.[1] The push toward more significant gains in energy storage capacity has led to interest in alternative battery systems, such as those storing charge through alternative processes.[2−5] Among these alternatives are materials that store charge by conversion,[6,7] in which extensive chemical and structural changes result in much higher theoretical capacities than the layered transition metal oxides that enable commercial LIBs. However, in practice conversion materials rarely achieve their theoretical capacity and tend to have poor reversibility, efficiency, and cycle life.

Various strategies have been employed to overcome these issues conversion materials face, especially particle engineering and the incorporation of specialty conductive additives or electrolyte formulations.[8−11] Concurrently, efforts are being made to elucidate the nature of charge storage in conversion-based electrochemical energy storage through detailed studies of micro/nanostructure and atomic structure evolution with cycling.[12−18]

From these a general equation has been established to describe the first discharge reaction of a compound M_aX_b (where M is a transition metal and X is an anion) with Li (eq 1):[6]

$$M_aX_b + (bn)\mathrm{Li}^+ + (bn)\mathrm{e}^- \rightarrow aM^0 + b\mathrm{Li}_nX \quad (1)$$

In practice, there are subtleties in the discharge that neither this nor any general reaction scheme capture. For example, there can be intermediate reactions during discharge and asymmetric phase evolution pathways on charge with the initial compound rarely being recovered upon charge. Further, there are many compounds that could store charge through this mechanism;[6] accordingly, it is challenging to anticipate the charge storage reaction(s) or performance of a conversion compound a priori.

To guide selection and design of promising conversion materials, we must first identify the impact of composition and structure on Li storage. Part of this understanding comes from characterizing average and local structure evolution during cycling and relating it to electrochemical features. In particular,

Received: August 11, 2018
Revised: October 6, 2018
Published: October 24, 2018

DOI: 10.1021/acs.jpcc.8b07828
J. Phys. Chem. C 2018, 122, 24559−24569

doing so over multiple cycles is critical for materials with assymmetric discharge and charge pathways and can even illuminate structural and chemical sources of capacity fade.[8,15,19,20] By sampling structure−composition effects in various families of conversion compounds, we can begin to illuminate the role of atomic species and initial structure on performance. This, in turn, can guide the community toward inherently better systems and strategies to approach the promise of high-capacity conversion materials.

With this in mind, we consider the cycling performance, modes of charge storage, and possible origins of capacity fade of CoS_2 as a cathode material. CoS_2 has the pyrite structure, which can be thought of as a face-centered cubic (*fcc*) sublattice of M^{2+}, with each M octahedrally coordinated by disulfide units (S_2^{2-}) [Figure 1a]. Drawing comparison to our previously published findings for FeS_2,[20] we find these isostructural sulfides, only with the difference of an extra electron on the transition metal, lead to surprising differences in performance.

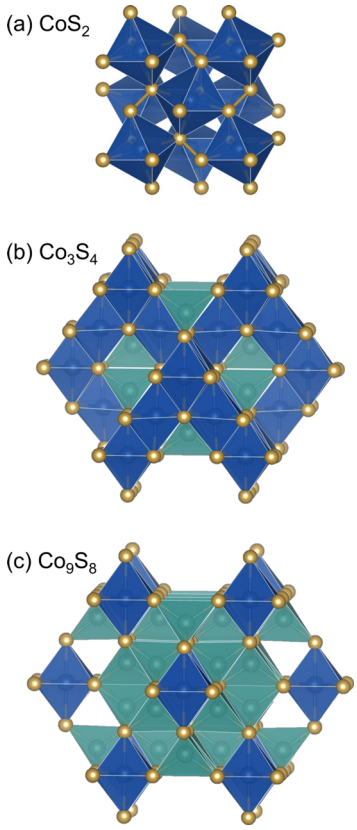

Figure 1. (a) CoS_2 ($Pa\bar{3}$)[21] is composed of an *fcc* lattice of Co^{2+} atoms (blue) octahedrally coordinated by S_2^{2-} disulfides. (b) In Co_3S_4 ($Fd\bar{3}m$)[22] spinel, Co^{3+} and Co^{2+} are, respectively, octahedrally (blue) and tetrahedrally coordinated (teal) by S. (c) In defect spinel Co_9S_8 ($Fm\bar{3}m$),[23] Co has an average oxidation state of 1.78+ and is tetrahedrally and octahedrally coordinated by S, with more tetrahedrally coordinated Co than Co_3S_4.

FeS_2 and CoS_2 were initially studied for use in high-temperature molten-salt batteries that operate at 350 °C and above for which phase evolution is anticipated to follow the ternary Li−M−S phase diagrams.[24−27] For both compounds, this involves the formation of Li_2S and binary transition metal sulfides, such as Fe_3S_4 and Co_3S_4 (Figure 1), with final discharge products of M and Li_2S. For CoS_2, complete discharge would involve reaction with 4 mol of Li (per mole of CoS_2) following eq 2:

$$CoS_2 + 4Li^+ + 4e^- \rightarrow Co^0 + 2Li_2S \quad (2)$$

On the basis of the ternary phase diagram, if the first discharge followed equilibrium conditions it would occur in several conversion steps (eqs 3, 4, and 5), the first of which would include an increase in Co oxidation state upon reducing S_2^{2-}.

$$CoS_2 + \frac{4}{3}Li^+ + \frac{4}{3}e^- \rightarrow \frac{1}{3}Co_3S_4 + \frac{2}{3}Li_2S \quad (3)$$

$$\frac{1}{3}Co_3S_4 + \frac{2}{3}Li_2S + \frac{8}{9}Li^+ + \frac{8}{9}e^- \rightarrow \frac{1}{9}Co_9S_8 + \frac{10}{9}Li_2S \quad (4)$$

$$\frac{1}{9}Co_9S_8 + \frac{10}{9}Li_2S + \frac{16}{9}Li^+ + \frac{16}{9}e^- \rightarrow Co^0 + 2Li_2S \quad (5)$$

The above reaction scheme is proposed for high-temperature CoS_2 and is extended in this case to carbonate-based electrolytes. In the case of an ether-based electrolyte, dissolution and enhanced redox activity of sulfur species would likely result in different or additional reaction processes.

Recent ambient temperature studies of pyrites for energy storage focus on FeS_2, which has better inherent performance than CoS_2. Such studies focus on structural evolution as well as strategies to augment performace through, for example, the use of solid[28] or ionic liquid[29] electrolytes. Despite the poor room-temperature performance of CoS_2 relative to FeS_2, improved performance of CoS_2 has been demonstrated by employing particle engineering and the addition of specialty carbons.[9,30−33] Even so, these reports see significant irreversible capacity in the first cycle and do not address the contributions of conductive carbon additives and electrolyte decomposition reactions to capacity at low potentials.[34]

The few published studies investigating the cycling products of CoS_2 rely on electron microscopy and X-ray diffraction (XRD).[32,35] Electron microscopy is useful for characterizing changes in particle shape and morphology, as well as cycling, and can also provide atomic structure insights.[13,17,32,36,37] XRD is useful in tracking changes of crystalline phases, but has limitations in studying conversion reactions in which initially crystalline materials quickly lose sufficient long-range order to be probed by XRD.[16,19,36] For the complete picture of conversion for an ensemble of particles, rather than the few that can be evaluated with transmission electron microscopy (TEM), other local structure probes can provide additional information. In particular, in or ex situ local structure methods including pair distribution function (PDF), X-ray absorption spectroscopy (XAS), and nuclear magnetic resonance (NMR) have been critical in expanding our understanding of conversion-type electrochemical reactions.[8,12,14,15] For CoS_2 in particular, Tao et al. observe changes not captured by XRD in the local Co coordination environment of CoS_2 with cycling using Co *K*-edge X-ray absorption near-edge spectroscopy (XANES).[33]

Here, we investigate the structural evolution with cycling using PDF analysis from operando X-ray total scattering and ex situ XANES relating our findings to previous studies of this system as well as our prior work on FeS_2. We find atomic and nanostructural phenomena that contribute to the drastic differences in performance of FeS_2 and CoS_2, including distinct

DOI: 10.1021/acs.jpcc.8b07828
J. Phys. Chem. C 2018, 122, 24559−24569

types of intermediate products and possible capacity fade mechanisms.

2. METHODS

2.1. Ex Situ Cell Assembly, Cycling, and Sample Preparation. Cycling was carried out in Swagelok cells with loose-powder electrodes of CoS_2 (Sigma-Aldrich, 99.98%) and conductive carbon additive Ketjen Black (KB) (AkzoNobel EC-600JD) in a 9:1 ratio by weight. Powders were ground by hand with an agate mortar and pestle. $LiPF_6$ (1 M) in ethylene carbonate:dimethyl carbonate (EC:DMC) (1:1 ratio by volume) electrolyte (Aldrich) and two glass fiber Whatman GFD separators were used. Li metal served as a counter and reference electrode in these half-cells. Cells were assembled in an Ar glovebox and cycled galvanostatically at $C/40$ ($Q/10$), calculated for the theoretical reaction of CoS_2 with 4 mol of Li in 40 h, with potential limitations of 1 and 3 V for discharge and charge, respectively. Cells were cycled using a Bio-Logic VMP-3. Li−FeS_2 cells were prepared and tested in the same manner, as described previously.[20]

For ex situ XANES, loose-powder Swagelok cells were cycled to a specified potential or capacity limit and disassembled in an Ar glovebox. The collected cathode powders were washed with DMC and dried under vacuum. Dried powders were painted into homogeneous films on kapton tape and transported under Ar.

2.2. Ex Situ XANES. Ex situ Co *K*-edge XANES was measured at 20-BM-B at the Advanced Photon Source at Argonne National Laboratory for cells cycled at $C/40$, as described above. XANES spectra were collected in transmission mode, calibrated to 7.709 keV,[38] and normalized by aligning the E_0 for each Co foil to a reference spectra. Data was deglitched, normalized, and averaged using the open source program ATHENA.[39]

2.3. Operando PDF. Operando total scattering experiments were carried out at 11-ID-B at the Advanced Photon Source at Argonne National Laboratory. A Perkin-Elmer amorphous Si-based area detector enabled rapid acquisition of X-ray scattering measurements with an X-ray wavelength of 0.2112 Å (about 58 keV). An AMPIX electrochemical cell[40] was assembled in an Ar glovebox with a free-standing film cathode composed of CoS_2:graphite/VulcanC (1:1 ratio by weight):-polytetrafluoroethylene (PTFE) (70:20:10% by weight). The free-standing film cathode was 13 mm in diameter and about 160 μm thick. The electrolyte was 1 M $LiPF_6$ in EC:DMC in a 3:7 ratio by volume, which soaked a GFD separator. Li metal served as a counter and reference electrode.

The cell was galvanostatically cycled with an applied current of 0.8228 mA for a *C* rate of about $C/18$ based on the reaction of 1 mol of CoS_2 with 4 mol of Li and with potential limits of 1 and 3 V. Due to constraints on acquisition time, faster cycling was used for operando than for ex situ cycling to ensure the collection of PDF beyond the first cycle.

The background contribution of the operando cell was collected for an AMPIX cell assembled without a cathode. Experimental geometries were calibrated using CeO_2 powder and Fit2D freeware.[41] Fit2D was also used to integrate 2D data from X-ray total scattering, which was collected every 30 min during cycling. From each set of integrated data, the real-space PDF was calculated by the Fourier transform with the structure factor accounting for the approximate Li content and a constant molar Co:S ratio of 1:2 and with a q_{max} = 19 Å^{-1}. Least-squares methods were used to fit real space PDF data to known structures using PDFgui.[42] Crystal structure visualizations were prepared using VESTA 3.[43]

OriginPro was used for linear combination analysis (LCA) of operando PDF data. From least-squares fitting of the initial material, the first discharge product, the first charge product, and the fifth charge product, simulated patterns of refined local structures were simulated and used as "components" to fit measured data using multiple linear regression function analysis. The components were fit using least-squares refinements in which scale, lattice parameters, particle size (as spdiameter), and in some cases U_{iso} and a correlated motion parameter, delta, were refined.

3. RESULTS

3.1. Cycling of CoS_2. Galvanostatic cycling of unoptimized loose-powder Swagelok cells shows two plateaus over the first discharge and charge [Figure 2a]. As early as the second charge, however, plateaus become much less well defined and there is significant capacity fade by the third charge (Figure 2).

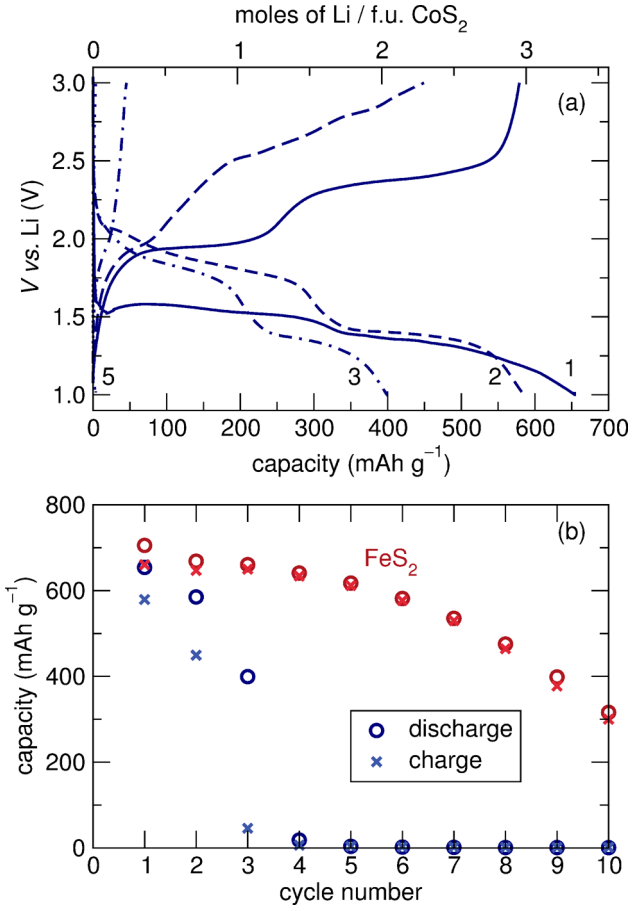

Figure 2. (a) Galvanostatic cycling of loose-powder Swagelok cells of CoS_2:Ketjen Black (9:1 by weight) vs Li shows two plateaus on discharge and charge. Later cycles are shown as increasingly broken lines, as labeled. Ssecond charge has much less well-defined plateaus, and third charge has significant capacity fade. (b) Capacity per cycle shows a marked difference in capacity retention and the nature of capacity fade: gradual for FeS_2 (red) and primarily upon charge for CoS_2 (blue).

The dramatic contrast in capacity retention with cycling for CoS_2 and FeS_2 is unexpected given they are isostructural, have the same anion, and have a difference of only an electron between the Fe and the Co [Figure 2b]. Even so, FeS_2 maintains a higher capacity for longer with capacity retention of

DOI: 10.1021/acs.jpcc.8b07828
J. Phys. Chem. C 2018, 122, 24559−24569

87.5% and 44.8% for the fifth and tenth cycles, respectively, and the nature of the capacity fade is different from that of CoS_2. FeS_2 loses some capacity every cycle, with most of the discharge capacity recovered on charge. In contrast, CoS_2 suffers significant capacity fade in the first few charges with <1% capacity retention by the fifth cycle. Further, the capacity is overwhelmingly lost due to irreversibility upon charge.

3.2. Ex Situ XANES. Ex situ Co *K*-edge XANES was carried out at various states of charge to probe the oxidation state and local environment of Co during the cycling of secondary Li–CoS_2 cells. Halfway through the first discharge (at the end of the first plateau [yellow in Figure 3a]), the edge shifts to lower

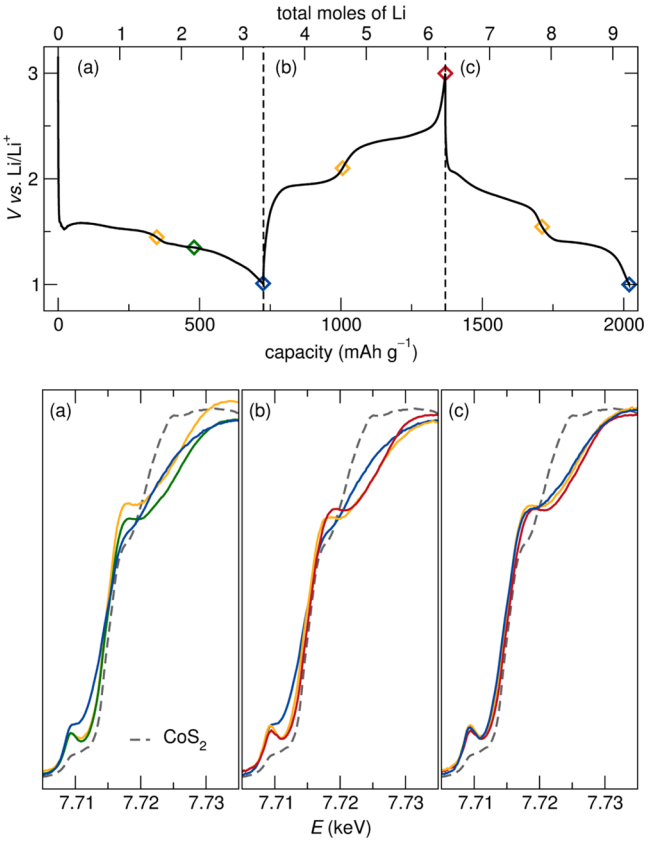

Figure 3. (Top) First 1.5 cycles of Li–CoS_2 cells stopped at various states of charge, as marked, and (bottom) Co *K*-edge XANES of CoS_2 and at each state of charge. Colors of the lines in the lower panel correspond to the colors of the shapes in the upper panel. Most notable evolution is the pre-edge peak at intermediate and charged states in (a and b) the first cycle and throughout (c) the second discharge, which indicates tetrahedrally coordinated Co.

E relative to CoS_2 and a pre-edge peak develops. The pre-edge feature indicates the presence of tetrahedrally coordinated Co, arising from the allowed 1s to 3d transition, which is disallowed in octahedral coordination environments.[44,45] With continued reduction a product partway through the second plateau of the first discharge maintains the pre-edge peak at 7.709 keV, indicating tetrahedrally coordinated Co is still present [green in Figure 3a]. Additionally, the decreased slope of the edge indicates the reduction of Co. At the end of discharge, the near-edge features are similar to those of Co but differ from the bulk metal [blue in Figure 3a]. This is in agreement with our previous observations for the Fe metal clusters formed at the end of the first discharge of FeS_2.[20]

During the first charge the intermediate and charge products have a pre-edge peak, intermediate slopes, and an edge step similar to the intermediates of the first discharge [yellow in Figure 3b]. The charge product has a slightly larger step height, and the edge is shifted to higher *E*, indicating more oxidized Co than the intermediate.[44] XANES reveals that CoS_2 does not form upon charge.

During the second discharge, there are only minor changes to the edge, pre-edge, and postedge, including slight shifts of the edge to lower *E* with reduction [Figure 3c]. XANES also shows Co metal, even as small disordered clusters, is not the majority product of the second discharge, in contrast to the first discharge.

From XANES we see changes in the local coordination environment of Co during the first cycle. In particular, we see intermediates and a first charge product with some tetrahedrally coordinated Co. The first discharge product has Co metal but in sufficiently small and disordered clusters that the XANES is unique from that of bulk Co. During the second discharge, however, there are only minor changes the local environment of Co, despite an appreciable measured capacity of about 2 mol of Li per mole of CoS_2, and XANES indicates the presence of Co tetrahedrally and octahedrally coordinated by S throughout the second discharge. This is suggestive of a spinel-like local structure, such as Co_3S_4 or Co_9S_8.

3.3. Operando PDF Data and Least-Squares Analysis. PDF data from X-ray total scattering was collected for a Li–CoS_2 cell for 10 cycles at a rate of about *C*/18 (based on the reaction of 4 mol of Li per mole of CoS_2 in 18 h). The electrochemical curves from the AMPIX cell are consistent with those measured for loose-powder Swagelok cells with slightly less well-defined plateaus on the first discharge [Figures 2 and 4a]. Significant capacity fade in the first three cycles was also similar to ex situ cycling. In the following we discuss the local structure evolution during the first 1.5 cycles and structural analysis at specific states of charge.

The pristine material [Figure 4(i)] is fit well to CoS_2 before cycling (R_w = 0.137) [Figure 5a, Table 1]. Over the first plateau of the first discharge [Figure 4(i–ii)] there is conversion from CoS_2 to a new local structure. Also, the decrease in intensity of

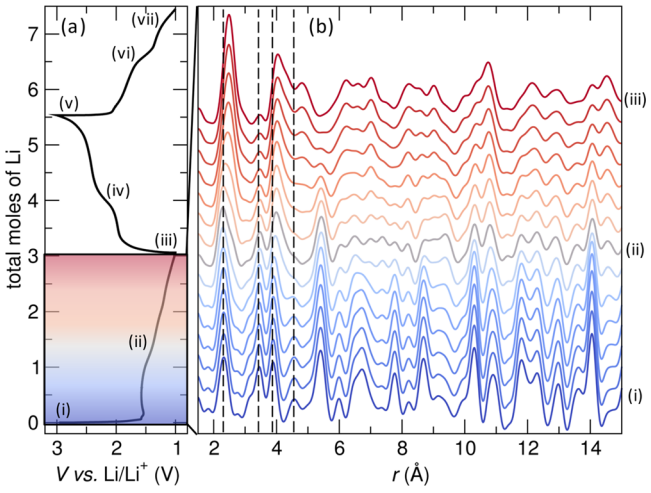

Figure 4. (a) First 1.5 cycles of an operando Li–CoS_2 cell, and (b) PDF data collected during the first discharge (i–iii). Dashed lines correspond to the first four prominent correlations of CoS_2, highlighting changes in positions and intensities of peaks over the first discharge.

DOI: 10.1021/acs.jpcc.8b07828
J. Phys. Chem. C 2018, 122, 24559–24569

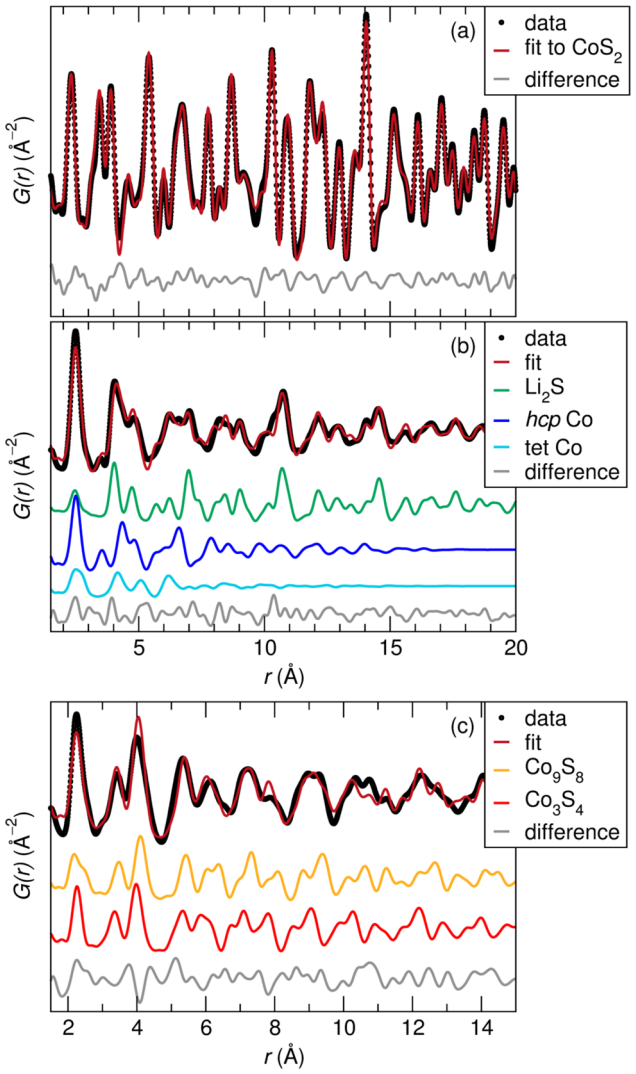

Figure 5. (a) PDF data before cycling is fit to CoS_2 ($Pa\bar{3}$). (b) PDF data for the first discharge product it fit by Li_2S and Co metal. Contributions of Li_2S ($Fm\bar{3}m$) as well as *hcp* ($P6_3/mmc$) and tet Co ($P4_2/mnm$) are shown. Damping corresponds to particle diameters of about 45 Å for Li_2S and 20 Å for Co. (c) PDF data of the first charge product is fit to Co_3S_4 ($Fd\bar{3}m$) and Co_9S_8 ($Fm\bar{3}m$) with particle diameters of about 30 Å. (Fits shown here were refined using least-squares methods; for multiphase fits, the contributions of each phase are shown.)

correlations at higher *r* indicates a decrease in the domain size and crystallinity of the intermediate and discharge products relative to micrometer-sized particles of CoS_2 before cycling. Using the dashed lines that mark the first four major peaks of CoS_2 for reference, from i to ii a shoulder at higher *r* develops on the first peak, the second and third peaks shift to higher *r*, and the fourth peak decreases in intensity. Over the remainder of the discharge, another local structure evolves [Figure 4(ii–iii)], highlighted by the disappearance of the first peak and a shift to a correlation at higher *r* with increased intensity near the first dashed line. Also, from ii to iii the intensity at the second dashed line decreases and the correlation near the third dashed line continues to shift to higher *r*. Comparing the PDF data in Figure 4b at i, ii, and iii, we see two steps in the local structure evolution over the first discharge. These changes are consistent with our findings from ex situ Co *K*-edge XANES over the first discharge, which also suggests distinct intermediate and first discharge products.

In fitting PDF data of poorly crystalline materials, a few caveats should be considered: the structures we describe (Table 1) do not occur as bulk phases; we capture the features of the local structure, but there are residual differences; residual correlations leave the possibility of deviations from the structures we report; fitting parameters required for this type of analysis can be highly correlated. Even so, through least-squares fitting we identify local structure motifs at various states of charge that aid in understanding the observed performance of CoS_2 under these cycling conditions, especially in combination with linear combination analysis (LCA) and Co *K*-edge XANES.

The local structure features of the first discharge product can be captured by a combination of Li_2S and small clusters of Co metal (Figure 5b). Both hexagonal close-packed (*hcp*) Co ($P6_3/mmc$, ICSD collection code 44990[48]) and tetragonal (tet) Co ($P4_2/mnm$, ICSD collection code 165725[47]) (Table 1) are required to capture the local correlations, which do not quite resemble more typical *hcp* or *fcc* structures of Co. The tet Co is based on the sigma phase, a brittle alloy that can act as a crack nucleation site in welded stainless steels.[47] We do not observe this structure as a bulk phase, though we do find the local correlations of calculated tet Co capture the measured local structure of the discharge product. It is possible that this structure is descriptive of disordered, nanoscale clusters of Co or else the interface between *hcp* Co clusters and Li_2S. The observation of disordered metal clusters at the end of a conversion reaction discharge, as we find here, has been reported for a number of other systems employing local structure methods.[15,19,20] A three-phase fit of the PDF data with Li_2S and ∼20 Å clusters of *hcp* and tet Co captures the local structure features of the first discharge product (Figure 5b, Table 1).

The first charge of operando PDF takes place over two plateaus and involves significant changes to the local structure [Figure 5(iii-v)], suggestive of two reactions, one over each plateau. We see a new correlation near the first dashed line at lower *r* over the first plateau as well as changes in the position and intensity of correlations near the second and third dashed lines [Figure 6b(iii–iv)]. Local correlations near the dashed

Table 1. Table of Structures Used to Fit PDF before Cycling, at the First Discharge, and at the First Charge (Figure 4a, 4b, and 4c)[a]

	before cycling	discharge					charge	
fit to	CoS_2[21]	Li_2S[46]	tet Co[47]		*hcp* Co[48]		Co_3S_4[22]	Co_9S_8[23]
lp	*a* (Å)	*a* (Å)	*a* (Å)	*c* (Å)	*a* (Å)	*c* (Å)	*a* (Å)	*a* (Å)
published	5.5385	5.7600	8.4244	4.4557	2.5054	4.0893	9.4055	9.9280
refined	5.5299	5.7004	8.6246	4.5572	2.5103	4.1311	9.5133	9.7940
% difference	−0.155	−1.035	2.377	2.277	0.196	1.023	1.146	−1.350

[a]Lattice parameters (lp) from the literature and refined here, as well as the percent difference between them, are provided for each fit.

DOI: 10.1021/acs.jpcc.8b07828
J. Phys. Chem. C 2018, 122, 24559−24569

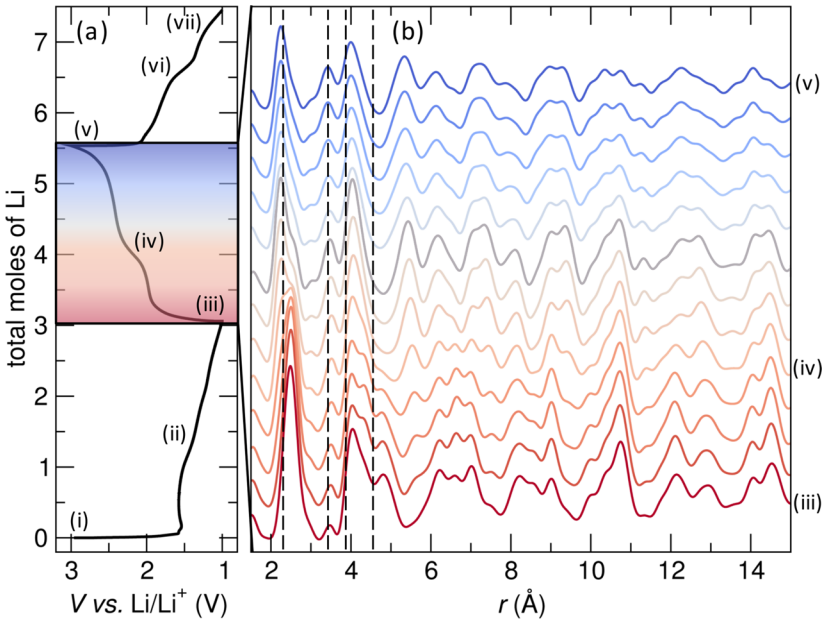

Figure 6. (a) First 1.5 cycles of an operando Li−CoS_2 cell, and (b) PDF data collected during the first charge (iii−v). Dashed lines correspond to the first four prominent correlations of CoS_2 and are referenced in the text to highlight changes in the positions and intensities of peaks over the first charge as well as to emphasize that CoS_2 is not recovered upon charge.

lines also highlight changes over the second plateau of the first charge [Figure 6 (iv−v)]. The charge product [Figure 5b(v)] has a local structure distinct from that of CoS_2, which is highlighted by the dashed lines that mark the positions of the first four major correlations for CoS_2. The local structure of the first charge product can be fit by a combination of Co_3S_4 and Co_9S_8 [Figure 5c, Table 1]. Given the combination of octahedrally and tetrahedrally coordinated Co in these phases (Figure 1), PDF and ex situ XANES analyses are in agreement.

Similar to the first charge, the second discharge takes place over two plateaus [Figure 7a(v−vii)], although these are less

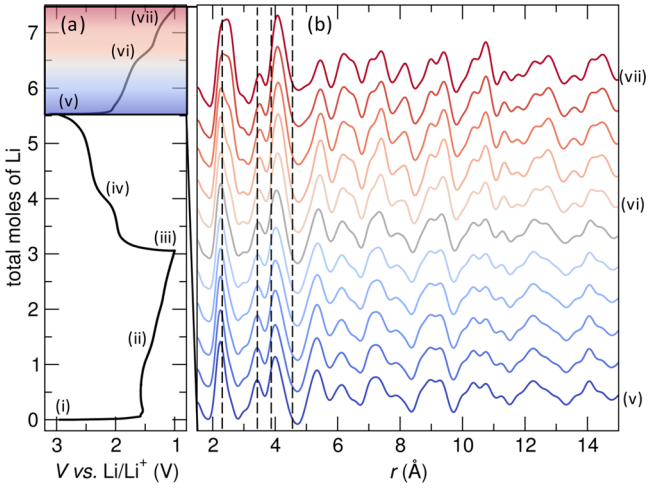

Figure 7. (a) First 1.5 cycles of operando Li−CoS_2 cell, and (b) PDF data collected during the second discharge (v−vii). Dashed lines correspond to the first four prominent correlations of CoS_2 and are included to highlight changes in the positions and intensities of low *r* correlations over the second discharge.

well defined and more sloped than those of the first charge. Over the higher potential plateau, centered at about 2.5 V, changes in the local structure are subtle [Figure 7(v−vi)] and the local structure at the end of the second discharge [Figure 7b(vii)] is different from that of the first discharge product [Figure 4b(iii)]. Even so, changes to the local structure below 5 Å are relatively minor, in agreement with XANES data, which shows only subtle changes in the local coordination environment of Co over the second discharge.

In cycling beyond the second charge, the local correlations in the operando PDF data are relatively unchanged as the capacity quickly fades. The discharge and charge products of the third and later cycles are nearly identical (Figure 8). PDF of the fifth charge product is fit by 45 Å diameter particles of defect spinel Co_9S_8 and 60 Å diameter particles of disordered Li_2S (Figure 9).

3.4. Linear Combination Analysis of Operando PDF Data. PDF data was collected at 50+ states of charge over multiple cycles, each with at least two local structures required to capture correlations. As mentioned, in least-squares fitting of this type of data multiple refinement parameters [lattice parameter, U_{iso}, correlation parameters (delta), and particle diameter (as spdiameter)] can be correlated, especially for multiple phases, adding complexity as well as uncertainty to refinements. To avoid overfitting data, LCA was used to qualitatively visualize the evolution of contributions from multiple local structures during cycling.

LCA in combination with principle component analysis (PCA) has previously been employed for the efficient analysis of PDF data from in situ and operando electrochemical cycling experiments.[50] From comparing PDF data to simulated pairwise correlations of known phases and fitting data at various states of charge we had a general idea of the local structures that could be present throughout cycling. Accordingly, we used local structure patterns from least-squares fits at more well-defined (fewer phases) states of charge as the "components" rather than defining them from PCA.

For our components we used fits to data before cycling to CoS_2: the first discharge product to Li_2S and a combination of *hcp* and tet Co; the first charge to Co_3S_4 and Co_9S_8; and the

DOI: 10.1021/acs.jpcc.8b07828
J. Phys. Chem. C 2018, 122, 24559−24569

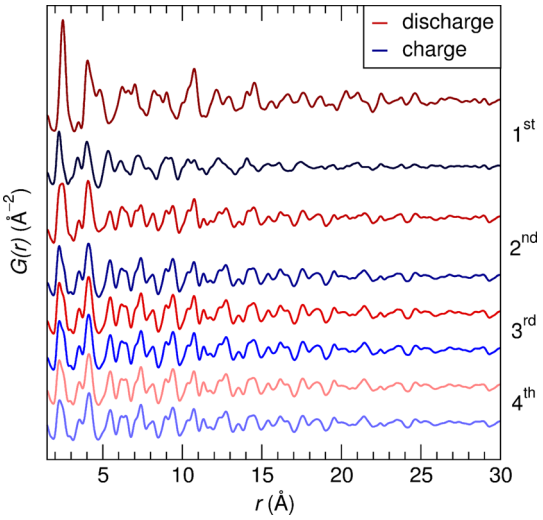

Figure 8. PDF data of discharge (red) and charge products (blue) of the first four cycles. Beyond the second cycle, changes in the PDF are negligible and capacity is low.

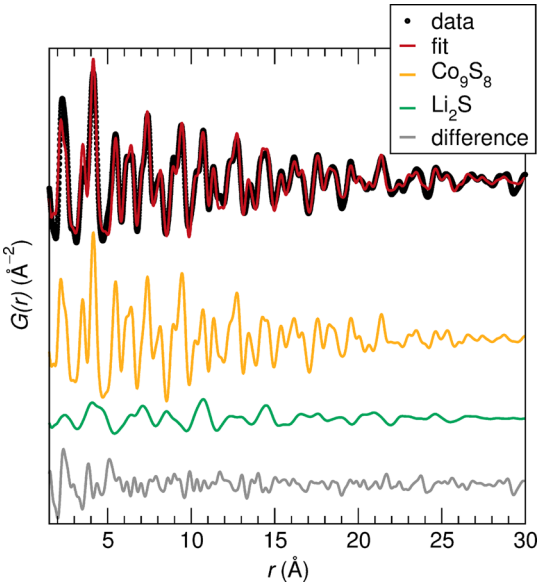

Figure 9. PDF data of the fifth charge product is fit to Co_9S_8 (particle diameter 45 Å) and Li_2S (particle diameter 60 Å). Contributions of each local structure and the difference between the data and fit are shown.

fifth charge product to Co_9S_8 and Li_2S. From these CoS_2 fit before cycling, Li_2S, *hcp* Co, and tet Co fit to the first discharge product, Co_3S_4 fit to the first charge product, and Co_9S_8 fit to the fifth charge product were simulated and used as the components for LCA.

LCA with all of the components resulted in nonphysical negative weightings at some states of charge. Accordingly, certain components were excluded from LCA for these states of charge in which case various subsets of components were evaluated for LCA. In particular, only one spinel-like local structure (Co_9S_8) was used for LCA of the first discharge. Also, the component weightings are not representative of phase fraction but do aid in visualizing the production or consumption of a local structure with cycling. For example, for the first discharge product, LCA shows a 2:1 ratio of Co metal to Li_2S, whereas we expect a 1:2 molar ratio based on eq 1. Additionally, at the beginning of cycling LCA shows about 15% weighting of tet Co [Figure 10(left)] even though least-squares refinement shows a good fit for CoS_2 alone (Figure 5a). This is likely a consequence of the disordered nature of tet Co relative to the other components, which could cause it to be artificially weighted to minimize residuals. Despite the limitations this illustrates, we find good agreement of trends of local structure evolution from LCA with electrochemical features (Figure 10), least-squares analysis of PDF data, and XANES.

Over the first plateau of the first discharge, LCA shows the formation of a Co_9S_8-like local structure at the expense of CoS_2 [Figure 10(left)]. Over the second plateau of the first discharge, Co_9S_8 and the remaining CoS_2 are reacted with Li to form Co metal clusters and Li_2S [Figure 10(left)]. During the first charge, LCA shows the formation of Co_9S_8 at the expense of Co metal and Li_2S over the first plateau [Figure 10(center)]. Over the second plateau, Li_2S and some Co_9S_8 are consumed during the formation of Co_3S_4. However, at the end of charge, there are still contributions of Co_9S_8.

The weightings of Co_3S_4 and Co_9S_8 are fairly constant over the first plateau of the second discharge, corresponding to the reaction of about 1 mol of Li per mole of CoS_2 [Figure 10(right)]. As the second discharge continues, Co_3S_4 is consumed during the formation of Co_9S_8. Over the lower plateau, some Co_9S_8 is converted to Co metal and Li_2S. At the end of the second discharge, however, about one-half of the Co_9S_8 that formed intermediately remains.

An unexpected feature of LCA is the rather constant weighting of Li_2S over the second discharge, which we would anticipate to increase with reduction [Figure 10(right)]. This might indicate the incorporation of Li into the sulfide spinels, which has been reported for Co_3O_4 and other oxide spinels.[51]

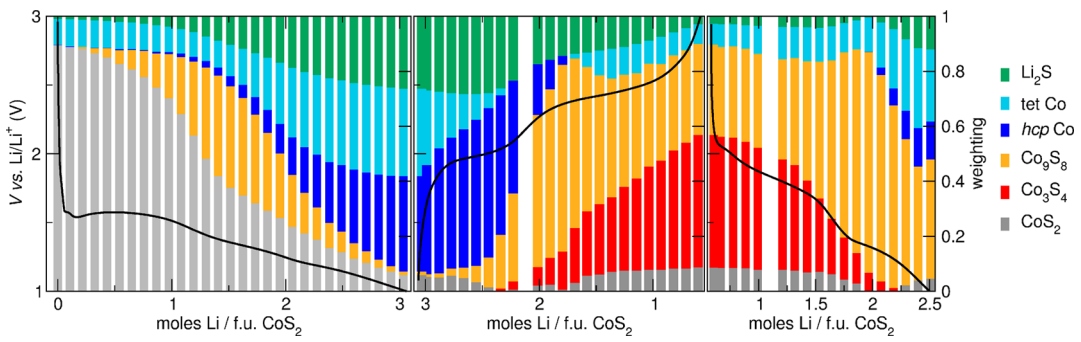

Figure 10. LCA shows the trends in structural evolution over the first 1.5 cycles of operando PDF. Weighting of components (right *y* axis) is shown as a function of Li content, and we see changes in ratios that correspond to the features of the potential curve (black, left *y* axis). Blank spaces are due to beam outages during the measurement.

DOI: 10.1021/acs.jpcc.8b07828
J. Phys. Chem. C 2018, 122, 24559−24569

However, confirming this for Co_9S_8- or Co_3S_4-like local structures would require a more targeted study.

LCA of subsequent charge and discharge products shows the weighting of Co_9S_8 stays fairly constant over each cycle (Figure 11). The accumulation of Co_9S_8 is concurrent with

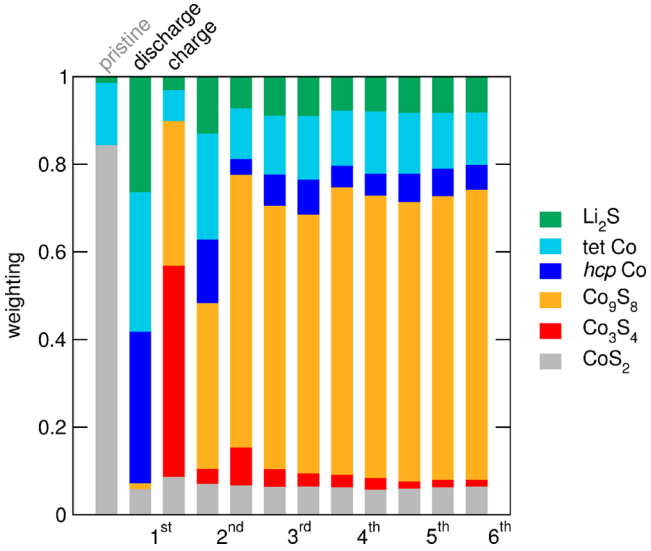

Figure 11. LCA of the cathode before cycling and at each discharge and charge from operando PDF summarizes the products of each cycle. After the second charge, the capacity significantly fades and the product is primarily composed of Li_2S and Co_9S_8.

a fade of capacity to about 0.2 mol of Li per mole of CoS_2 (0.13 mol of Li per mole of Co_9S_8). This fade in capacity is accompanied by only subtle changes in the weighting of local structure components beyond the second charge (Figure 11).

4. DISCUSSION

For conversion reaction electrode materials the utility of combining local structure methods to understand the nature of charge storage or capacity fade has been established. With this in mind, we supplement previous studies of CoS_2 for Li-based electrochemical energy storage. Optimization through nanostructuring and modification with conductive carbon have been previously reported, as have structural evolution studies using XRD, TEM, or XAS. For the first time, we combine X-ray PDF from total scattering with Co *K*-edge XANES and are able to better understand the modes of charge storage and capacity fade for CoS_2 cycled under these conditions. At elevated temperatures or with ether-based electrolytes, the processes likely vary. LCA of PDF data enables us to qualitatively describe local structure evolution with cycling, especially relating electrochemical features with structure changes. While LCA as used here is quantitatively limited, in combination with least-squares fits of PDF data as well as XANES at specific states of charge we shed light on the nature of reactions during charge storage and propose failure modes based on our analyses.

4.1. First Discharge. Results of least-squares fitting of the initial active material and the first discharge product are consistent with expectations based on the conversion reaction model, following eq 2. Some caveats for CoS_2, however, are that the products that form are not crystalline but rather are disordered local structures that resemble those crystalline phases. In particular, we find the metal that forms at the end of discharge is disordered and has small domains, on the order of nanometers. The pairwise correlations of these domains are captured in least-squares fitting using a combination of stable *hcp* and a metastable tetragonal Co with particle diameters on the order of 10−20 Å. LCA shows that Li_2S and a spinel-like local structure, captured by the Co_9S_8-like component, form intermediately during the first discharge. Both the intermediate and the discharge products from operando PDF data, analyzed by least-squares and LCA, are in agreement with Co *K*-edge XANES, which has a pre-edge feature indicating the presence of tetrahedrally coordinated Co intermediately and an edge similar to but distinct from bulk Co metal at the end of the first discharge.

These findings differ from proposed reaction schemes in the literature that suggest CoS_2 initially intercalates Li to form Li_xCoS_2 over the first plateau before conversion to Co and Li_2S over the second.[35] While it is possible that a modest amount of Li may be accommodated by CoS_2 before the nucleation of other local structures, the intercalation over the first plateau, accounting for 1.5−2 mol of Li per mole of CoS_2, is unlikely. This conclusion is drawn by Yan et al. based on the absence of new peaks in in situ XRD during the first discharge,[35] but it has since been established that conversion reaction products typically lack sufficient long-range order to be detected using XRD.[15,19,36] In our PDF data we see changes in the local structure during the first half of the first discharge, but they are more extensive than we would expect for the intercalation of Li into CoS_2. As discussed, Co tetrahedrally coordinated by S, as apparent in ex situ XANES, suggests more extensive structural changes take place during the first discharge than would be expected for an intercalation-type lithiation mechanism. Tao et al. see a similar pre-edge feature in Co *K*-edge XANES partway through the first discharge of CoS_2.[33]

4.2. First Charge. During the first charge, LCA shows the conversion of Li_2S and Co metal to Co_9S_8 in the first half of the discharge. Over the second plateau, Li_2S continues to be consumed as Co_3S_4 begins to form. Some Co_9S_8 is also consumed in favor of Co_3S_4, resulting in a combination of Co_3S_4-, Co_9S_8-, and Li_2S-like local structures at the end of the first charge. The presence of tetrahedrally coordinated Co in these spinel and defect-spinel structures is consistent with XANES partway through and at the end of the first charge. Least-squares fitting of the first charge product also shows a combination of Co_3S_4- and Co_9S_8-like local structures. Neither XANES nor PDF suggest the formation of CoS_2 upon charge. The original compound not being reformed on charge is expected based on previous studies of conversion systems.[15,19,20]

4.3. Second Discharge. Over the first plateau of the second discharge LCA shows conversion of Co_3S_4 to Co_9S_8. Over the second plateau of the second discharge, Co and Li_2S form at the expense of some of the Co_9S_8 but the spinel-like structure persists through the second discharge. While we expect primarily Co metal and Li_2S, the apparent persistence of Co_9S_8 seen in LCA is consistent with the predominance of spinel-like features we see in XANES for the second discharge product.

The consistency of XANES over the second discharge despite reaction with over 3 mol of Li leaves is intriguing. Spinel transition metal oxides, especially of the form M_3O_4 such that M = Mn, Fe, or Co, have been found to accommodate some Li through the migration of M from tetrahedral to octahedral sites during lithiation.[51−54] Also, other oxide spinels have been extensively studied as intercalation electrodes, among them $Li_4Ti_5O_{12}$. In a study of the local coordination and oxidation

DOI: 10.1021/acs.jpcc.8b07828
J. Phys. Chem. C 2018, 122, 24559−24569

state of Ti in $Li_4Ti_5O_{12}$, the Ti *K*-edge underwent only subtle changes with cycling.[55] On the basis of behavior in oxides, it is possible that Li could be accommodated into the thiospinel structures and if this happened, that the metal edge may have only minor changes. However, to conclude if there is any host behavior by these or related thiospinels cannot be concluded from this data or analysis and would require a more targeted study.

4.4. Later Cycling. PDF data over subsequent cycles shows that a decrease in the extent of structural changes coincides with capacity fade. From the second charge and later, the weighting of Co_9S_8 is quite consistent. This suggests Co_9S_8 (or a spinel-like local structure) plays a role in the capacity fade under the employed conditions (carbonate electrolyte, *C*/18 and slower rates, room temperature, etc.). Co_9S_8 has been reported as a conversion electrode itself; however, intentional incorporation of carbon additives as well as control of particle size and shape are needed to realize useful capacity.[9,31,32] On the basis of our results and previous studies, the Co_9S_8-like local structure could be a poor Li^+ or e^- conductor. Alternatively, volume expansion could result in particle fracture, rendering the material electronically isolated and, thus, electrochemically inactive.[32] This would make sense based on other work in which the liftimes of transition metal sulfides are improved by the careful incorporation of conductive carbon additives and binders.[33] In our prevoius work on FeS_2, we found a correlation of capacity fade and the growth and stabilization of Fe metal clusters.[20] In combination with this study of CoS_2, this suggests that *M* and atomic structure are central factors impacting the extent and cause of capacity fade. Despite having the same initial structure, we identify differences in the nature of intermediate products and find the relatively rapid capacity fade of CoS_2 coincides with the irreversible formation of Co_9S_8, though it is not clear why the Co_9S_8-like local structure is so detrimental to cycling.

5. CONCLUSIONS

We have described the evolution of the local structure of the cathode in secondary Li−CoS_2 cells based on ex situ XANES and operando PDF data, which is summarized in Figure 12.

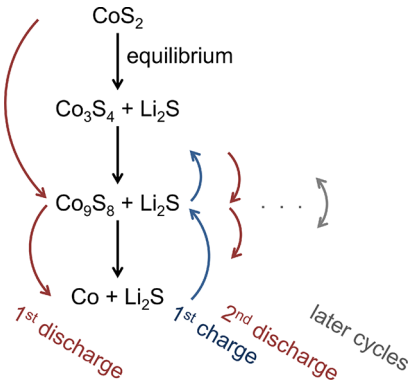

Figure 12. On the basis of the local structure characterization and analysis, we describe the reactions that occur upon reaction with Li in initial and later cycling relative to the reactions predicted by the equilibrium phase diagram.

We find cycling products have poor crystallinity, but the observed local structures can be modeled based on known binaries within the Li−Co−S ternary phase diagram. Other deviations from equilibrium products could involve thiospinels Co_3S_4 and Co_9S_8 accommodating Li, as has been observed for related oxide spinels, but this cannot be confirmed without further study.

On the first discharge, CoS_2 is converted to Li_2S and cobalt sulfide spinel, resembling Co_9S_8, and then to Li_2S and Co. In our PDF analysis, some equilibrium *hcp* Co is present, but there are also correlations captured by a metastable, tetragonal Co structure based on the sigma phase,[47,49] which could be reflective of disordered Co at the interface between *hcp* metal clusters and Li_2S. Over the first charge we see conversion to Co_9S_8 and Co_3S_4 during oxidation, but CoS_2 is not recovered. The second discharge follows the reverse of the first charge but without complete conversion to Co metal. With continued cycling capacity fade is correlated with only minor structural changes and thus a small compositional range, as an electrochemically inactive product accumulates, which has a Co_9S_8-like local structure.

We find differences in the reaction modes and local structure evolution of CoS_2 relative to previously studied FeS_2, which stores charge through mixed conversion and intercalation-like modes. Also, while spinel-like products are associated with rapid capacity fade for CoS_2, we find the eventual accumulation of Fe metal contributes to gradual capacity fade for FeS_2. For CoS_2, we find the local structure evolution is similar to that described by the ternary phase diagram with deviations from the bulk phases, possibly to metastable structures such as tet Co and Li-containing thiospinel derivatives.

This work highlights the role of local structure methods in understanding the observed cycling behavior of conversion electrode materials. We identify modes of charge storage distinct from other structurally and chemically related conversion materials. Additionally, this work in combination with previous reports challenges some long-standing assumptions regarding the modes of charge storage and failure mechanisms that plague conversion electrode performance. For example, the metal clusters that form with discharge are apparently not the primary cause of capacity fade and irreversibility—in contrast to intuition. Rather, for CoS_2 capacity fade is associated with the formation of binary products with local structures resembling Co_4S_4 and Co_98_8. Further, the lack of long-range order of cycling products does not necessarily contribute to poor cycling; rather, the formation of relatively stable, electrochemically inactive intermediates appears to be more problematic for capacity retention.

For a given conversion electrode material, the size and local structure of cycling products will vary with conditions of rate, temperature, initial particle size and morphology, as well as choice of electrolyte−particularly for sulfides. We hope these findings drive further understanding of transition metal sulfides for conversion-based energy storage, including methods of selecting and screening promising candidates for high-capacity secondary energy storage.

AUTHOR INFORMATION

Corresponding Authors

*E-mail: mbutala@umail.ucsb.edu.
*E-mail: seshadri@mrl.ucsb.edu.

ORCID

Megan M. Butala: 0000-0002-7759-5300
Vicky V. T. Doan-Nguyen: 0000-0003-4204-3271
Karena W. Chapman: 0000-0002-8725-5633
Ram Seshadri: 0000-0001-5858-4027

DOI: 10.1021/acs.jpcc.8b07828
J. Phys. Chem. C 2018, 122, 24559−24569

Notes

The authors declare no competing financial interest.

■ ACKNOWLEDGMENTS

M.M.B. gratefully acknowledges support from the Fletcher Jones and Peter J. Frenkel Foundation fellowships. V.V.T.D.-N. is supported by the University of California Presidential Postdoctoral Fellowship and the UCSB California Nano-Systems Institute (CNSI) Elings Prize Fellowship and gratefully acknowledges the Southern California Electrochemical Energy Storage Alliance (SCEESA), supported by the UCSB CNSI. A.J.L. gratefully acknowledges support of the Swiss National Science Foundation Fellowship No. PBSKP2-145825. M.A.L. was supported by the RISE program through NSF-DMR 1121053. Experiments at UCSB made use of MRL facilities, supported by the MRSEC Program of the NSF under Grant No. NSF-DMR 1121053. This research made use of resources of the Advanced Photon Source, a U.S. Department of Energy (DOE) Office of Science User Facility operated for the DOE Office of Science by Argonne National Laboratory under Contract No. DE-AC02-06CH11357. X-ray absorption experiments were performed at APS 20-BM-B under GUP-41555. Sector 20 operations are supported by the US Department of Energy and the Canadian Light Source. X-ray scattering experiments were performed at APS 11-ID-B under GUP-45245. The authors thank Dr. Geneva Laurita and Professor Michael Hayward for useful discussions regarding PDF analysis and Li storage mechanisms in spinel structures, respectively.

■ REFERENCES

(1) Goodenough, J. B. Rechargeable Batteries: Challenges Old and New. *J. Solid State Electrochem.* **2012**, *16*, 2019−2029.
(2) Levi, E.; Gofer, Y.; Aurbach, D. On the Way to Rechargeable Mg Batteries: The Challenge of New Cathode Materials. *Chem. Mater.* **2010**, *22*, 860−868.
(3) Kim, S.-W.; Seo, D.-H.; Ma, X.; Ceder, G.; Kang, K. Electrode Materials for Rechargeable Sodium-Ion Batteries: Potential Alternatives to Current Li-Ion Batteries. *Adv. Energy Mater.* **2012**, *2*, 710−721.
(4) Wu, X.; Leonard, D. P.; Ji, X. Emerging Non-Aqueous Potassium-Ion Batteries: Challenges and Opportunities. *Chem. Mater.* **2017**, *29*, 5031−5042.
(5) Ponrouch, A.; Palacín, M. R. On the Road Toward Calcium-Based Batteries. *Curr. Opin. Electrochem.* **2018**, *9*, 1−7.
(6) Cabana, J.; Monconduit, L.; Larcher, D.; Palacín, M. R. Beyond Intercalation-Based Li-Ion Batteries: The State of the Art and Challenges of Electrode Materials Reacting Through Conversion Reactions. *Adv. Mater.* **2010**, *22*, E170−E192.
(7) Balaya, P.; Li, H.; Kienle, L.; Maier, J. Fully Reversible Homogeneous and Heterogeneous Li Storage in RuO_2 with High Capacity. *Adv. Funct. Mater.* **2003**, *13*, 621−625.
(8) Britto, S.; Leskes, M.; Hua, X.; Hébert, C.-A.; Shin, H. S.; Clarke, S.; Borkiewicz, O.; Chapman, K. W.; Seshadri, R.; Cho, J.; et al. Multiple Redox Modes in the Reversible Lithiation of High-Capacity, Peierls-Distorted Vanadium Sulfide. *J. Am. Chem. Soc.* **2015**, *137*, 8499−8508.
(9) Luo, W.; Xie, Y.; Wu, C.; Zheng, F. Sperical CoS_2@Carbon Core-Shell Nanoparticles: One-Pot Synthesis and Li Storage Properties. *Nanotechnology* **2008**, *19*, 075602.
(10) Su, Q.; Du, G.; Zhang, J.; Zhong, Y.; Xu, B.; Yang, Y.; Neupane, S.; Kadel, K.; Li, W. *In Situ* Transmission Electron Microscopy Investigation of the Electrochemical Lithiation−Delithation of Individual Co_9S_8/Co-Filled Carbon Nanotubes. *ACS Nano* **2013**, *7*, 11379−11387.
(11) Zhang, S. S.; Tran, D. T. Mechanism and Solution for the Capacity Fading of Li/FeS_2 Battery. *J. Electrochem. Soc.* **2016**, *163*, A792−A797.
(12) Wiaderek, K. M.; Borkiewicz, O. J.; Pereira, N.; Ilavsky, J.; Amatucci, G. G.; Chupas, P. J.; Chapman, K. W. Mesoscale Effects in Electrochemical Conversion: Coupling of Chemistry to Atomic- and Nanoscale Structure in Iron-Based Electrodes. *J. Am. Chem. Soc.* **2014**, *136*, 6211−6214.
(13) Wang, F.; Yu, H.-C.; Van der Ven, A.; Thornton, K.; Pereira, N.; Zhu, Y.; Amatucci, G. G.; Graetz, J. Ionic and Electronic Transport in Metal Fluoride Conversion Electrodes. *ECS Trans.* **2013**, *50*, 19−25.
(14) Hua, X.; Robert, R.; Du, L.-S.; Wiaderek, K. M.; Leskes, M.; Chapman, K. W.; Chupas, P. J.; Grey, C. P. Comprehensive Study of the CuF_2 Conversion Reaction Mechanism in a Lithium Ion Battery. *J. Phys. Chem. C* **2014**, *118*, 15169−15184.
(15) Lowe, M. A.; Gao, J.; Abruña, H. D. In Operando X-ray Studies of the Conversion Reaction in Mn_3O_4 Lithium Battery Anodes. *J. Mater. Chem. A* **2013**, *1*, 2094−2103.
(16) See, K. A.; Leskes, M.; Griffin, J.; Britto, S.; Matthews, P.; Emly, A.; Van der Ven, A.; Wright, D.; Morris, A.; Grey, C. P.; et al. Ab Initio Structure Search and In Situ 7Li NMR Studies of Discharge Products in the Li−S Battery System. *J. Am. Chem. Soc.* **2014**, *136*, 16368−16377.
(17) McDowell, M. T.; Lu, Z.; Koski, K. J.; Yu, J. H.; Zheng, G.; Cui, Y. In Situ Observation of Divergent Phase Transformations in Sulfide Nanocrystals. *Nano Lett.* **2015**, *15*, 1264−1271.
(18) Hwang, S.; Yao, Z.; Zhang, L.; Fu, M.; He, K.; Mai, L.; Wolverton, C.; Su, D. Multistep Lithiation of Tin Sulfide: An Investigation Using In Situ Electron Microscopy. *ACS Nano* **2018**, *12*, 3638−3645.
(19) Boesenberg, U.; Marcus, M. A.; Shukla, A. K.; Yi, T.; McDermott, E.; Teh, P. F.; Srinivasan, M.; Moewes, A.; Cabana, J. Asymmetric Pathways in the Electrochemical Conversion Reaction of NiO as Battery Electrode with High Storage Capacity. *Sci. Rep.* **2015**, *4*, 7133.
(20) Butala, M. M.; Mayo, M.; Doan-Nguyen, V. V. V. T.; Lumley, M. A.; Göbel, C.; Wiaderek, K. M.; Borkiewicz, O. J.; Chapman, K. W.; Chupas, P. J.; Balasubramanian, M.; et al. Local Structure Evolution and Modes of Charge Storage in Secondary Li−FeS_2 Cells. *Chem. Mater.* **2017**, *29*, 3070−3082.
(21) Nowack, E.; Schwarzenbach, D.; Hahn, T. Charge Densitites in CoS_2 and NiS_2 (Pyrite Structure). *Acta Crystallogr., Sect. B: Struct. Sci.* **1991**, *47*, 650−659.
(22) Knop, O.; Reid, K.; Sutarno, R.; Nakagawa, Y. Chalkogenides of the Transition Elements. VI. X-ray, Neutron, and Magnetic Investigation of the Spinels Co_3S_4, $NiCo_2O_4$, and $NiCo_2S_4$. *Can. J. Chem.* **1968**, *46*, 3463−3476.
(23) Geller, S. Refinement of the Crystal Structure of Co_9S_8. *Acta Crystallogr.* **1962**, *15*, 1195−1198.
(24) Preto, S. K.; Tomczuk, Z.; von Winbush, S.; Roche, M. R. Reactions of FeS_2, CoS_2, and NiS_2 Electrodes in Moleten LiCl−KCl Electrolytes. *J. Electrochem. Soc.* **1983**, *130*, 264−273.
(25) Masset, P. J.; Guidotti, R. A. Thermally Activated ("Thermal") Battery Technology PartIIIa: FeS_2 Cathode Material. *J. Power Sources* **2008**, *177*, 595−609.
(26) Masset, P. J.; Guidotti, R. A. Thermally Activated ("Thermal") Battery Technology PartIIIb: Sulfur and Oxide-based Cathode Materials. *J. Power Sources* **2008**, *178*, 456−466.
(27) Keller, P.; Smith, P.; Winchester, C.; Papadakis, N.; Barlow, G.; Shuster, N. Rechargeable Fused Salt Batteries for Undersea Vehicles. *Proceedings of the 38th Power Sources Conference*; 1998.
(28) Yersak, T. A.; Macpherson, H. A.; Kim, S. C.; Le, V.-D.; Kang, C. S.; Son, S.-B.; Kim, Y.-H.; Trevey, J. E.; Oh, K. H.; Stoldt, C.; et al. Solid State Enabled Reversible Four Electron Storage. *Adv. Energy Mater.* **2013**, *3*, 120−127.
(29) Evans, T.; Piper, D. M.; Kim, S. C.; Han, S. S.; Bhat, V.; Oh, K. H.; Lee, S.-H. Ionic Liquid Enabled FeS_2 for High-Energy-Density Lithium-Ion Batteries. *Adv. Mater.* **2014**, *26*, 7386−7392.

DOI: 10.1021/acs.jpcc.8b07828
J. Phys. Chem. C 2018, 122, 24559−24569

(30) Wang, Q.; Jiao, L.; Han, Y.; Du, H.; Peng, W.; Huan, Q.; Song, D.; Si, Y.; Wang, Y.; Yuan, H. CoS_2 Hollow Spheres: Fabrication and Their Application in Lithium-Ion Batteries. *J. Phys. Chem. C* **2011**, *115*, 8300−8304.
(31) Xie, J.; Liu, S.; Cao, G.; Zhu, T.; Zhao, X. Self-assembly of CoS_2/Graphene Nanoarchitecture by a Facile One-Pot Route and its Improved Electrochemical Li-Storage Properties. *Nano Energy* **2013**, *2*, 49−56.
(32) Su, Q.; Xie, J.; Zhang, J.; Zhong, Y.; Du, G.; Xu, B. In Situ Transmission Electron Microscopy Obersvation of Electrochemical Behavior of CoS_2 in Lithium-Ion Battery. *ACS Appl. Mater. Interfaces* **2014**, *6*, 3016−3022.
(33) Tao, S.; Huang, W.; Xie, H.; Zhang, J.; Wang, Z.; Chu, W.; Qian, B.; Song, L. Formation of Graphene-encapsulated CoS_2 Hybrid Composites with Hierarchical Structures for High-performance Lithium-ion Batteries. *RSC Adv.* **2017**, *7*, 39427−39433.
(34) See, K. A.; Lumley, M.; Stucky, G. D.; Grey, C. P.; Seshadri, R. Reversible Capacity of Conductive Carbon Additives at Low Potentials: Caveats for Testing Alternative Anode Materials for Li-Ion Batteries. *J. Electrochem. Soc.* **2017**, *164*, A327−A333.
(35) Yan, J. M.; Huang, H. Z.; Zhang, J.; Liu, Z. J.; Yang, Y. A Study of the Novel Anode Material CoS_2 for Lithium Ion Battery. *J. Power Sources* **2005**, *146*, 264−269.
(36) Butala, M. M.; Danks, K. R.; Lumley, M. A.; Zhou, S.; Melot, B. C.; Seshadri, R. MnO Conversion in Li-Ion Batteries: In Situ Studies and the Role of Mesostructuring. *ACS Appl. Mater. Interfaces* **2016**, *8*, 6496−6503.
(37) Yamakawa, N.; Jiang, M.; Key, B.; Grey, C. P. Identifying the Local Structures Formed during Lithation of the Conversion Material, Iron Fluoride, in a Li Ion Battery: A Solid-State NMR, X-ray Diffraction, and Pair Distribution Function Analysis Study. *J. Am. Chem. Soc.* **2009**, *131*, 10525−10536.
(38) Thompson, A.; Attwood, D.; Gullikson, E.; Howells, M.; Kim, K.-J.; Kirz, J.; Kortright, J.; Lindau, I.; Pianetta, P.; Robinson, A. et al. *X-ray Data Booklet*; Lawrence Berkeley National Lab: Berkeley, 2009, 1−2.
(39) Ravel, B.; Newville, M. ATHENA, ARTEMIS, HEPHAESTUS: Data Analysis for X-ray Absorption Spectroscopy Using IFEFFIT. *J. Synchrotron Radiat.* **2005**, *12*, 537−541.
(40) Borkiewicz, O. J.; Shyam, B.; Wiaderek, K. M.; Kurtz, C.; Chupas, P. J.; Chapman, K. W. The AMPIX Electrochemical Cell: a Versatile Apparatus for *In Situ* X-ray Scattering and Spectroscopic Measurements. *J. Appl. Crystallogr.* **2012**, *45*, 1261−1269.
(41) Hammersley, A. P.; Svensson, S. O.; Hanfland, M.; Fitch, A. N.; Hausermann, D. Two-Dimensional Detector Software: From Real Detector to Idealised Image or Two-Theta Scan. *High Pressure Res.* **1996**, *14*, 235−248.
(42) Farrow, C. L.; Juhas, P.; Liu, J. W.; Bryndin, D.; Bozin, E. S.; Bloch, J.; Proffen, T.; Billinge, S. J. L. PDFfit2 and PDFgui: Computer Programs for Studying Nanostructure in Crystals. *J. Phys.: Condens. Matter* **2007**, *19*, 335219.
(43) Momma, K.; Izumi, F. VESTA 3 for Three-Dimensional Visualization of Crystal, Volumetric, and Morphology Data. *J. Appl. Crystallogr.* **2011**, *44*, 1272−1276.
(44) Shulman, R. G.; Yafet, Y.; Eisenberger, P.; Blumberg, W. E. Observation and Interpretation of X-ray Absorption Edges in Iron Compounds and Proteins. *Proc. Natl. Acad. Sci. U. S. A.* **1976**, *73*, 1384−1388.
(45) Bouwens, S. M. A. M.; Koningsberger, D. C.; de Beer, V. H. J.; Prins, R. The Structure of the Cobalt Sulfide Phase in Carbon-Supported Co and Co−Mo Sulfide Catalysts as Studied by EXAFS and XANES. *Catal. Lett.* **1988**, *1*, 55−59.
(46) Buehrer, W.; Altorfer, F.; Mesot, J.; Bill, H.; Carron, P.; Smith, H. G. Lattice Dynamics and the Diffuse Phase Transition of Lithium Sulphide Investigated by Coherent Neutron Scattering. *J. Phys.: Condens. Matter* **1991**, *3*, 1055−1064.
(47) Pavlü, J.; Vřeštál, J.; Šob, M. Ab Initio Study of the Formation Energy and Magnetism of Sigma Phase in Cr−Fe and Fe−Co Systems. *Intermetallics* **2010**, *18*, 212−220.
(48) Owen, E. A.; Jones, D. M. Effect of Grain Size on the Crystal Structure of Cobalt. *Proc. Phys. Soc., London, Sect. B* **1954**, *67*, 456−466.
(49) Heino, S.; Knutson-Wedel, E. M.; Karlsson, B. Precipitation Behaviour in Heat Affected Zone of Welded Superaustenitic Stainless Steel. *Mater. Sci. Technol.* **1999**, *15*, 101−108.
(50) Chapman, K. W.; Lapidus, S. H.; Chupas, P. J. Applications of Principal Component Analysis to Pair Distribution Function Data. *J. Appl. Crystallogr.* **2015**, *48*, 1619−1626.
(51) Thackeray, M. M.; Baker, S. D.; Adendorff, K. T.; Goodenough, J. B. Lithium Insertion into Co_3O_4: A Preliminary Investigation. *Solid State Ionics* **1985**, *17*, 175−181.
(52) Thackeray, M. M.; David, W. I. F.; Bruce, P. G.; Goodenough, J. B. Lithium Insertion into Manganese Spinels. *Mater. Res. Bull.* **1983**, *18*, 461−472.
(53) Thackeray, M. M.; David, W. I. F.; Goodenough, J. B. Structural Characterization of the Lithiated Iron Oxides $Li_xFe_3O_4$ and $Li_xFe_2O_3$ ($0 < x < 2$). *Mater. Res. Bull.* **1982**, *17*, 785−793.
(54) Hayward, M. In *Comprehensive Inorganic Chemistry*, 2nd ed.; Reedijk, J., Poeppelmeier, K., Eds.; Elsevier: Amsterdam, 2013; pp 417−453.
(55) Zhang, W.; Topsakal, M.; Cama, C.; Pelliccione, C. J.; Zhao, H.; Ehrlich, S.; Zhu, Y.; Frenkel, A. I.; Takeuchi, K. J.; Takeuchi, E. S.; et al. Multi-Stage Structural Transformations in Zero-Strain Lithium Titanate Unveiled by in Situ X-ray Absorption Finger-prints. *J. Am. Chem. Soc.* **2017**, *139*, 16591−16603.

DOI: 10.1021/acs.jpcc.8b07828
J. Phys. Chem. C 2018, 122, 24559−24569